

Neutral pion cross section and spin asymmetries at intermediate pseudorapidity in polarized proton collisions at $\sqrt{s} = 200$ GeV

L. Adamczyk,¹ J. K. Adkins,²³ G. Agakishiev,²¹ M. M. Aggarwal,³⁵ Z. Ahammed,⁵⁴ I. Alekseev,¹⁹ J. Alford,²² C. D. Anson,³² A. Aparin,²¹ D. Arkhipkin,⁴ E. C. Aschenauer,⁴ G. S. Averichev,²¹ J. Balewski,²⁷ A. Banerjee,⁵⁴ B. Barber,⁵³ Z. Barnovska,¹⁴ D. R. Beavis,⁴ R. Bellwied,⁵⁰ M. J. Betancourt,²⁷ A. Bhasin,²⁰ A. K. Bhati,³⁵ P. Bhattarai,⁴⁹ H. Bichsel,⁵⁶ J. Bielcik,¹³ J. Bielcikova,¹⁴ L. C. Bland,⁴ I. G. Bordyuzhin,¹⁹ W. Borowski,⁴⁶ J. Bouchet,²² A. V. Brandin,³⁰ A. Bridgeman,² S. G. Brovko,⁶ S. Bültmann,³³ I. Bunzarov,²¹ T. P. Burton,⁴ J. Butterworth,⁴¹ H. Caines,⁴⁸ M. Calderón de la Barca Sánchez,⁶ D. Cebra,⁶ R. Cendejas,³⁶ M. C. Cervantes,⁴⁸ P. Chaloupka,¹³ Z. Chang,⁴⁸ S. Chattopadhyay,⁵⁴ H. F. Chen,⁴³ J. H. Chen,⁴⁵ L. Chen,⁹ J. Cheng,⁵¹ M. Cherney,¹² A. Chikanian,⁵⁸ W. Christie,⁵⁸ J. Chwastowski,¹¹ M. J. M. Coddington,⁴⁹ R. Corliss,²⁷ J. G. Cramer,⁵⁶ H. J. Crawford,⁵ X. Cui,⁴³ S. Das,¹⁶ A. Davila Leyva,⁴⁹ L. C. De Silva,⁵⁰ R. R. Debbé,⁴ T. G. Dedovich,²¹ J. Deng,⁴⁴ A. A. Derevschikov,³⁷ R. Derradi de Souza,⁸ S. Dhamija,¹⁸ B. di Ruzza,⁴ L. Didenko,⁴ C. Dilks,³⁶ F. Ding,⁶ A. Dion,⁴ P. Djawotho,⁴⁸ X. Dong,²⁶ J. L. Drachenberg,⁵³ J. E. Draper,⁶ C. M. Du,²⁵ L. E. Dunkelberger,⁷ J. C. Dunlop,⁴ L. G. Efimov,²¹ J. Engelage,⁵ K. S. Engle,⁵² G. Eppley,⁴¹ L. Eun,²⁶ O. Evdokimov,¹⁰ R. Fatemi,²³ S. Fazio,⁴ J. Fedorisin,²¹ R. G. Fersch,²³ P. Filip,²¹ E. Finch,⁵⁸ Y. Fisyak,⁴ C. E. Flores,⁶ C. A. Gagliardi,⁴⁸ D. R. Gangadharan,³² D. Garand,³⁸ F. Geurts,⁴¹ A. Gibson,⁵³ M. Girard,⁵⁵ S. Gliske,² D. Grosnick,⁵³ Y. Guo,⁴³ A. Gupta,²⁰ S. Gupta,²⁰ W. Guryn,⁶ B. Haag,⁶ O. Hajkova,¹³ A. Hamed,⁴⁸ L.-X. Han,⁴⁵ R. Haque,³¹ J. W. Harris,⁵⁸ J. P. Hays-Wehle,²⁷ W. He,¹⁸ S. Heppelmann,³⁶ A. Hirsch,³⁸ G. W. Hoffmann,⁴⁹ D. J. Hofman,¹⁰ S. Horvat,⁵⁸ B. Huang,⁴ H. Z. Huang,⁷ P. Huck,⁹ T. J. Humanic,³² G. Igo,⁷ W. W. Jacobs,¹⁸ H. Jang,²⁴ C. Jena,³¹ E. G. Judd,⁵ S. Kabana,⁴⁶ D. Kalinkin,¹⁹ K. Kang,⁵¹ K. Kauder,¹⁰ H. W. Ke,⁹ D. Keane,²² A. Kechechyan,²¹ A. Kesich,⁶ Z. H. Khan,¹⁰ D. P. Kikola,³⁸ I. Kisel,¹⁵ A. Kisiel,⁵⁵ D. D. Koetke,⁵³ T. Kollegger,¹⁵ J. Konzer,³³ I. Koralt,³³ W. Korsch,²³ L. Kotchenda,³⁰ P. Kravtsov,³⁰ K. Krueger,² I. Kulakov,¹⁵ L. Kumar,²² R. A. Kycia,¹¹ M. A. C. Lamont,⁴ J. M. Landgraf,⁴ K. D. Landry,⁷ J. Lauret,⁴ A. Lebedev,⁴ R. Lednicky,²¹ J. H. Lee,⁴ W. Light,²⁷ M. J. LeVine,⁴³ C. Li,⁴³ W. Li,⁴⁵ X. Li,³⁸ X. Li,⁴⁷ Y. Li,⁵¹ Z. M. Li,⁹ L. M. Lima,⁴² M. A. Lisa,³² F. Liu,⁹ T. Ljubicic,⁴ W. J. Llope,⁴¹ R. S. Longacre,⁴ X. Luo,⁹ G. L. Ma,⁴⁵ Y. G. Ma,⁴⁵ D. M. M. D. Madagodagettige Don,¹² D. P. Mahapatra,¹⁶ R. Majka,⁵⁸ R. Manweiler,⁵³ S. Margetis,²² C. Markert,⁴⁹ H. Masui,²⁶ H. S. Matis,²⁶ D. McDonald,⁴¹ T. S. McShane,¹² N. G. Minaev,³⁷ S. Mioduszewski,⁴⁸ B. Mohanty,³¹ M. M. Mondal,⁴⁸ D. A. Morozov,³⁷ M. G. Munhoz,⁴² M. K. Mustafa,²⁶ M. Naglis,²⁶ B. K. Nandi,¹⁷ Md. Nasim,³¹ T. K. Nayak,⁵⁴ J. M. Nelson,³ L. V. Nogach,³⁷ S. Y. Noh,²⁴ P. M. Nord,⁵³ J. Novak,²⁹ S. B. Nurushev,³⁷ G. Odyniec,²⁶ A. Ogawa,⁴ K. Oh,³⁹ A. Ohlson,⁵⁸ V. Okorokov,³⁰ E. W. Oldag,⁴⁹ R. A. N. Oliveira,⁴² D. Olson,²⁶ M. Pachr,¹³ B. S. Page,¹⁸ S. K. Pal,⁵⁴ Y. X. Pan,⁷ Y. Pandit,¹⁰ Y. Panebratsev,²¹ T. Pawlak,⁵⁵ B. Pawlik,³⁴ H. Pei,⁹ C. Perkins,⁵ W. Peryt,⁵⁵ A. Peterson,³² P. Pile,⁴ M. Planinic,⁵⁹ J. Pluta,⁵⁵ D. Plyku,³³ W. Pochron,⁵³ N. Poljak,⁵⁹ J. Porter,²⁶ A. M. Poskanzer,²⁶ C. B. Powell,²⁶ C. Pruneau,⁵⁷ N. K. Pruthi,³⁵ M. Przybycien,¹ P. R. Pujahari,¹⁷ J. Putschke,⁵⁷ H. Qiu,²⁶ S. Ramachandran,²³ R. Raniwala,⁴⁰ S. Raniwala,⁴⁰ R. L. Ray,⁴⁹ C. K. Riley,⁵⁸ H. G. Ritter,²⁶ J. B. Roberts,⁴¹ O. V. Rogachevskiy,²¹ J. L. Romero,⁶ J. F. Ross,¹² A. Roy,⁵⁴ L. Ruan,⁴ J. Rusnak,¹⁴ N. R. Sahoo,⁵⁴ P. K. Sahu,¹⁶ I. Sakrejda,²⁶ S. Salur,²⁶ A. Sandacz,⁵⁵ J. Sandweiss,⁵⁸ E. Sangaline,⁶ A. Sarkar,¹⁷ J. Schambach,⁴⁹ R. P. Scharenberg,³⁸ J. Schaub,⁵³ A. M. Schmah,²⁶ W. B. Schmidke,⁴ N. Schmitz,²⁸ J. Seger,¹² I. Selyuzhenkov,¹⁸ P. Seyboth,²⁸ N. Shah,⁷ E. Shalaliev,²¹ P. V. Shanmuganathan,²² M. Shao,⁴³ B. Sharma,³⁵ W. Q. Shen,⁴⁵ S. S. Shi,²⁶ Q. Y. Shou,⁴⁵ E. P. Sichtermann,²⁶ R. N. Singaraju,⁵⁴ M. J. Skoby,¹⁸ D. Smirnov,⁴ N. Smirnov,⁵⁸ D. Solanki,⁴⁰ P. Sorensen,⁴ U. G. deSouza,⁴² H. M. Spinka,² B. Srivastava,³⁸ T. D. S. Stanislaus,⁵³ J. R. Stevens,²⁷ R. Stock,¹⁵ M. Strikhanov,³⁰ B. Stringfellow,³⁸ A. A. P. Suaide,⁴² M. Sumera,¹⁴ X. Sun,²⁶ X. M. Sun,²⁶ Y. Sun,⁴³ Z. Sun,²⁵ B. Surrow,⁴⁷ D. N. Svirida,¹⁹ T. J. M. Symons,²⁶ A. Szanto de Toledo,⁴² J. Takahashi,⁸ A. H. Tang,⁴ Z. Tang,⁴³ T. Tarnowsky,²⁹ J. H. Thomas,²⁶ A. R. Timmins,⁵⁰ D. Tlusty,¹⁴ M. Tokarev,²¹ S. Trentalange,⁷ R. E. Tribble,⁴⁸ P. Tribedy,⁵⁴ B. A. Trzeciak,⁵⁵ O. D. Tsai,⁷ J. Turnau,³⁴ T. Ullrich,⁴ D. G. Underwood,² G. Van Buren,⁴ G. van Nieuwenhuizen,²⁷ J. A. Vanfossen, Jr.,²² R. Varma,¹⁷ G. M. S. Vasconcelos,⁸ A. N. Vasiliev,³⁷ R. Vertesi,¹⁴ F. Videbæk,⁴ Y. P. Vijoyi,⁵⁴ S. Vokal,²¹ S. A. Voloshin,⁵⁷ A. Vossen,¹⁸ M. Wada,⁴⁹ M. Walker,²⁷ F. Wang,³⁸ G. Wang,⁷ H. Wang,⁴ J. S. Wang,²⁵ Q. Wang,³⁸ X. L. Wang,⁴³ Y. Wang,⁵¹ Y. Wang,¹⁰ G. Webb,²³ J. C. Webb,⁴ G. D. Westfall,²⁹ H. Wieman,²⁶ S. W. Wissink,¹⁸ R. Witt,⁵² Y. F. Wu,⁹ Z. Xiao,⁵¹ W. Xie,³⁸ K. Xin,⁴¹ H. Xu,²⁵ N. Xu,²⁶ Q. H. Xu,⁴⁴ W. Xu,⁷ Y. Xu,⁴³ Z. Xu,⁴ W. Yan,⁵¹ C. Yang,⁴³ Y. Yang,²⁵ Y. Yang,⁹ Z. Ye,¹⁰ P. Yepes,⁴¹ L. Yi,³⁸ K. Yip,⁴ I.-K. Yoo,³⁹ Y. Zawisza,⁴³ H. Zbroszczyk,⁵⁵ W. Zha,⁴³ J. B. Zhang,⁹ S. Zhang,⁴⁵ X. P. Zhang,⁵¹ Y. Zhang,⁴³ Z. P. Zhang,⁴³ F. Zhao,⁷ J. Zhao,⁴⁵ C. Zhong,⁴⁵ X. Zhu,⁵¹ Y. H. Zhu,⁴⁵ Y. Zoukarnieva,²¹ M. Zyzak¹⁵

(STAR Collaboration)

¹AGH University of Science and Technology, Cracow, Poland²Argonne National Laboratory, Argonne, Illinois 60439, USA³University of Birmingham, Birmingham, United Kingdom⁴Brookhaven National Laboratory, Upton, New York 11973, USA

- ⁵University of California, Berkeley, California 94720, USA
⁶University of California, Davis, California 95616, USA
⁷University of California, Los Angeles, California 90095, USA
⁸Universidade Estadual de Campinas, Sao Paulo, Brazil
⁹Central China Normal University (HZNU), Wuhan 430079, China
¹⁰University of Illinois at Chicago, Chicago, Illinois 60607, USA
¹¹Cracow University of Technology, Cracow, Poland
¹²Creighton University, Omaha, Nebraska 68178, USA
¹³Czech Technical University in Prague, FNSPE, Prague, 115 19, Czech Republic
¹⁴Nuclear Physics Institute AS CR, 250 68 Řež/Prague, Czech Republic
¹⁵Frankfurt Institute for Advanced Studies FIAS, Germany
¹⁶Institute of Physics, Bhubaneswar 751005, India
¹⁷Indian Institute of Technology, Mumbai, India
¹⁸Indiana University, Bloomington, Indiana 47408, USA
¹⁹Alikhanov Institute for Theoretical and Experimental Physics, Moscow, Russia
²⁰University of Jammu, Jammu 180001, India
²¹Joint Institute for Nuclear Research, Dubna, 141 980, Russia
²²Kent State University, Kent, Ohio 44242, USA
²³University of Kentucky, Lexington, Kentucky, 40506-0055, USA
²⁴Korea Institute of Science and Technology Information, Daejeon, Korea
²⁵Institute of Modern Physics, Lanzhou, China
²⁶Lawrence Berkeley National Laboratory, Berkeley, California 94720, USA
²⁷Massachusetts Institute of Technology, Cambridge, Massachusetts 02139-4307, USA
²⁸Max-Planck-Institut für Physik, Munich, Germany
²⁹Michigan State University, East Lansing, Michigan 48824, USA
³⁰Moscow Engineering Physics Institute, Moscow, Russia
³¹National Institute of Science Education and Research, Bhubaneswar 751005, India
³²Ohio State University, Columbus, Ohio 43210, USA
³³Old Dominion University, Norfolk, Virginia 23529, USA
³⁴Institute of Nuclear Physics PAN, Cracow, Poland
³⁵Panjab University, Chandigarh 160014, India
³⁶Pennsylvania State University, University Park, Pennsylvania 16802, USA
³⁷Institute of High Energy Physics, Protvino, Russia
³⁸Purdue University, West Lafayette, Indiana 47907, USA
³⁹Pusan National University, Pusan, Republic of Korea
⁴⁰University of Rajasthan, Jaipur 302004, India
⁴¹Rice University, Houston, Texas 77251, USA
⁴²Universidade de Sao Paulo, Sao Paulo, Brazil
⁴³University of Science and Technology of China, Hefei 230026, China
⁴⁴Shandong University, Jinan, Shandong 250100, China
⁴⁵Shanghai Institute of Applied Physics, Shanghai 201800, China
⁴⁶SUBATECH, Nantes, France
⁴⁷Temple University, Philadelphia, Pennsylvania 19122, USA
⁴⁸Texas A&M University, College Station, Texas 77843, USA
⁴⁹University of Texas, Austin, Texas 78712, USA
⁵⁰University of Houston, Houston, Texas 77204, USA
⁵¹Tsinghua University, Beijing 100084, China
⁵²United States Naval Academy, Annapolis, Maryland 21402, USA
⁵³Valparaiso University, Valparaiso, Indiana 46383, USA
⁵⁴Variable Energy Cyclotron Centre, Kolkata 700064, India
⁵⁵Warsaw University of Technology, Warsaw, Poland
⁵⁶University of Washington, Seattle, Washington 98195, USA
⁵⁷Wayne State University, Detroit, Michigan 48201, USA
⁵⁸Yale University, New Haven, Connecticut 06520, USA
⁵⁹University of Zagreb, Zagreb, HR-10002, Croatia

(Received 6 September 2013; published 15 January 2014)

The differential cross section and spin asymmetries for neutral pions produced within the intermediate pseudorapidity range $0.8 < \eta < 2.0$ in polarized proton-proton collisions at $\sqrt{s} = 200$ GeV are presented. Neutral pions were detected using the end cap electromagnetic calorimeter in the STAR detector at RHIC. The cross section was measured over a transverse momentum range of $5 < p_T < 16$ GeV/ c and is found to

agree with a next-to-leading order perturbative QCD calculation. The longitudinal double-spin asymmetry A_{LL} is measured in the same pseudorapidity range and spans a range of Bjorken- x down to $x \approx 0.01$. The measured A_{LL} is consistent with model predictions for varying degrees of gluon polarization. The parity-violating asymmetry A_L is also measured and found to be consistent with zero. The transverse single-spin asymmetry A_N is measured over a previously unexplored kinematic range in Feynman- x and p_T . Such measurements may aid our understanding of the onset and kinematic dependence of the large asymmetries observed at more forward pseudorapidity ($\eta \approx 3$) and their underlying mechanisms. The A_N results presented are consistent with a twist-3 model prediction of a small asymmetry over the present kinematic range.

DOI: 10.1103/PhysRevD.89.012001

PACS numbers: 21.10.Gv, 13.87.Ce, 13.88.+e, 14.20.Dh

I. INTRODUCTION

The production of π^0 mesons in $p + p$ collisions at $\sqrt{s} = 200$ GeV provides access to the combination of quark and gluon distribution functions within the proton, coupled with the fragmentation functions of the produced π^0 . For neutral pion production at $\sqrt{s} = 200$ GeV over the intermediate pseudorapidity range $0.8 < \eta < 2$ and the transverse momentum range $5 < p_T < 16$ GeV/ c the quark-gluon subprocess dominates over gluon-gluon and quark-quark subprocesses [1–3]. Previously published data on inclusive π^0 production in polarized proton-proton scattering have been at either central pseudorapidity ($-1 < \eta < 1$) [4–8] or at forward pseudorapidity ($\eta \approx 3$) [9–13]. The measurements described in this paper, taken at intermediate pseudorapidity, cover a less-constrained region of the Bjorken-scaling variable x and previously unmeasured regions of the Feynman- x and p_T kinematic domains. Feynman- x is defined as $x_F = 2p_L/\sqrt{s}$, where p_L represents the longitudinal momentum of the pion relative to the direction of the polarized beam.

Global analyses of fragmentation functions have shown that, due to increased sensitivity to gluonic scattering, RHIC measurements of inclusive pion production at central and forward pseudorapidity have been useful in constraining the gluon fragmentation function [14]. Since the present data span intermediate pseudorapidity and transverse momentum, they are expected to be sensitive to a different mix of partonic subprocesses than previous measurements at central and forward pseudorapidity. Thus, comparison of the present measured cross section to perturbative QCD (pQCD) calculations may aid current understanding of the gluon fragmentation function. Previous cross section measurements which span a similar range of p_T at central pseudorapidity [4,7,15] typically agree within the scale uncertainty of the pQCD prediction in the region of $5 < p_T < 16$ GeV/ c .

The longitudinal double-spin asymmetry A_{LL} is sensitive to the gluon polarization distribution $\Delta g(x)$ [16]. While $\Delta g(x)$ in the range $0.05 < x < 0.2$ has become more constrained [17,18], less is known for $x < 0.05$. As two protons are involved in the collision, there are two x values. We denote the larger x value as x_1 and the smaller as x_2 . In quark-gluon scattering, x_1 is most often associated with the quark and

x_2 with the gluon, since gluons dominate proton distribution functions at lower x . The production of π^0 mesons with $0.8 < \eta < 2.0$ at $\sqrt{s} = 200$ GeV covers approximately the range $0.1 < x_1 < 0.5$ and $0.01 < x_2 < 0.33$, with x_1 and x_2 increasing with p_T . Figure 1 shows Bjorken x_1 and x_2 distributions for two representative p_T bins, based on simulations using PYTHIA 6.423 [19] with tune “Pro-pT0” [20] utilizing the CTEQ5L set of unpolarized parton distribution functions [21].

Measurements of transverse single-spin asymmetries A_N for inclusive π^0 production [6], as well as inclusive jet production [22], at central pseudorapidity have shown no sizable effects. However, sizable asymmetries are observed for inclusive π^0 production at forward pseudorapidity ($\eta \approx 3$) by several experiments over a wide range of \sqrt{s} with no sign of \sqrt{s} dependence [9,11,13,23–25]. It is expected that the Sivers and Collins effects at twist-2 [26–30] as well as higher twist effects [31–34] contribute to these asymmetries (in particular at higher \sqrt{s}), and measurements which map the dependence in x_F and p_T may help elucidate the underlying mechanisms. While at large p_T , A_N is expected to scale as $1/p_T$ [29,30,35,36], previous results at forward pseudorapidity do not exhibit this behavior [23–25]. At intermediate p_T , the behavior is unknown. Model predictions also differ on the expected

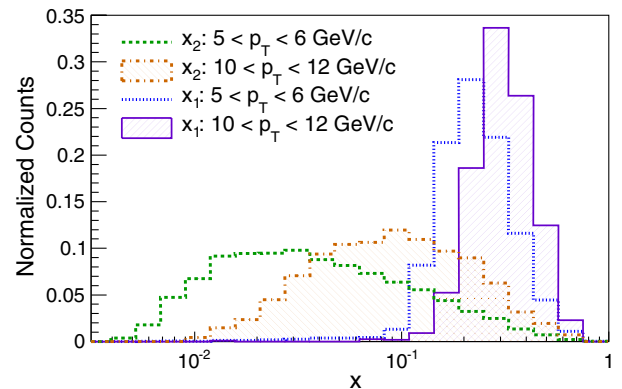


FIG. 1 (color online). Distributions of x_1 and x_2 in two different bins of reconstructed $\pi^0 p_T$ for events at $\sqrt{s} = 200$ GeV over $0.8 < \eta < 2$. The distributions were made using Monte Carlo simulations based on PYTHIA [19,20], utilizing unpolarized parton distribution functions.

behavior of A_N as a function of p_T . For example, while a recent model prediction based on the Collins effect in the color-glass condensate formalism [30] expects a $1/p_T$ scaling modified by the transverse-momentum dependence of the fragmentation function in the unpolarized cross section, a recent twist-3 model [34] predicts A_N of a few percent at forward pseudorapidity that should persist out to $p_T \sim 15$ GeV/ c . The A_N measurements described in this paper cover the previously unmeasured region $0.06 < x_F < 0.27$ and $5 < p_T < 12$ GeV/ c .

II. ANALYSIS

The data used for these measurements were taken with the STAR detector [37] during the 2006 RHIC run. The data for the cross section were extracted from a sampled luminosity of 8.0 pb $^{-1}$, while the data for the longitudinal and transverse asymmetries were extracted from sampled luminosities of 4.8 and 2.8 pb $^{-1}$, respectively. The vertex positions were determined using charged particle tracks in the time projection chamber (TPC) [38]. The beam-beam counters (BBCs) [39] were used to determine luminosity and were required in the event trigger.

The end cap electromagnetic calorimeter (EEMC) is used to measure the energy and position of photons from π^0 decays across the range of $1.086 < \eta_{\text{det}} < 2.00$, where η_{det} is the detector η , relative to the nominal interaction point. The EEMC is a lead-scintillator sampling calorimeter [40], with both of the first two layers and last layer being read out independently as preshower and postshower layers, respectively. Each layer in the EEMC consists of 720 independent segments formed from 12 sections in pseudorapidity (η) and 60 sections in azimuth (ϕ). The segments in all layers corresponding to a specific (η, ϕ) range, when taken together, are called a ‘‘tower.’’ A shower maximum detector (SMD) is located between layers five and six (at a depth of ~ 5 radiation lengths) and consists of two layers of tightly packed triangularly shaped scintillating strips ~ 1 cm wide at the base.

Photons are reconstructed by first clustering the energy depositions in the SMD strips to determine the position in η and ϕ and then using the corresponding EEMC towers to measure the photon energy. The EEMC detector components are calibrated using the most probable value of the Landau-peak response for minimum ionizing particles. Only SMD energy clusters with at least 3 MeV of deposited energy and at least 2 MeV deposited in the central strip of the cluster were used for this analysis. Clusters are seven strips in size and are required to have at least five strips with nonzero energy. The photon energy is determined by summing the energy in a 3×3 set of towers. In the case where a given tower is associated with more than one photon, the energy of the shared tower is distributed between the photons in a manner proportional to the energy each photon deposited in the SMD. Photons are further required to have an energy of at least 2.0 GeV as measured

in the associated tower(s) and to be within the fiducial volume of $1.11 < \eta_{\text{det}} < 1.96$. The physical η , determined relative to the TPC-reconstructed primary vertex, is required to be $0.8 < \eta < 2.0$. Further event selection requirements are (a) a valid bunch crossing (i.e. a bunch in both beams), (b) a TPC-reconstructed vertex within ± 120 cm of the nominal interaction point, (c) a π^0 candidate transverse momentum $p_T > 5$ GeV/ c , and (d) a summed preshower energy for each photon tower cluster of less than 40 MeV to exclude spurious events, e.g., beam gas and other noncollision background events. All possible pairs of photons that satisfy these requirements are considered as π^0 candidates.

The invariant mass of photon pairs can be expressed as

$$M_{\gamma\gamma} = (E_{\gamma_1} + E_{\gamma_2}) \sqrt{1 - z_{\gamma\gamma}^2} \sin \frac{\theta_{\gamma\gamma}}{2}, \quad (1)$$

where E_{γ_1} and E_{γ_2} represent the energies of the two photons, $z_{\gamma\gamma}$ represents the two-photon energy asymmetry $z_{\gamma\gamma} = |E_{\gamma_1} - E_{\gamma_2}| / (E_{\gamma_1} + E_{\gamma_2})$, and $\theta_{\gamma\gamma}$ represents the opening angle between the two photons. The limited photo-statistics in each SMD strip can cause a cluster of energy deposited by a single shower to appear as two clusters of energy and, thus, be reconstructed as two photons. This ‘‘false splitting’’ effect accounts for a large fraction of π^0 candidates with invariant mass below 0.1 GeV/ c^2 . False splitting can be somewhat mitigated by a ‘‘merging’’ procedure. Simulation studies indicate that when a false split results in multiple reconstructed pion candidates with $p_T > 4$ GeV/ c , the vast majority of candidates are reconstructed within a radius $\sqrt{\Delta\eta^2 + \Delta\phi^2} < 0.05$. Thus, if two π^0 candidates are found within a radius of 0.05, then these candidates are replaced with a new, merged candidate. The momentum of the merged candidate is set to the sum of the momenta of the contributing photons, without double counting photons that were included in the original π^0 candidates. Simulations indicate a potential loss of $\approx 0.13\%$ of events with $p_T > 4$ GeV/ c from merging two real pions, an effect considered negligible. The other large contributor to low mass π^0 candidates is the case in which one of the SMD clusters of a real π^0 is not reconstructed; and, thus, the reconstructed photon from the real pion is never paired with the correct second photon. The cluster may have been lost due to being below the energy threshold or, more frequently, due to two clusters merging in one of the layers. The real π^0 with the lost cluster will have its opening angle, and thus its mass, reconstructed lower than the true value.

Reconstruction of π^0 candidates with invariant mass above 0.2 GeV/ c^2 can arise from a conspiracy of two effects. Finite energy resolution affects the reconstruction of $z_{\gamma\gamma}$. Furthermore, when additional energy from the parent jet is deposited in the vicinity of the photon pair, the reconstruction algorithm may include this energy with that of the true pion. These two effects conspire to increase the

amount of π^0 signal reconstructed with mass above the peak region.

All events considered in this analysis are from a single trigger that includes a coincidence requirement in the two BBCs, implying a $p + p$ collision. The trigger requires at least one EEMC tower with transverse energy above a given threshold and with the total transverse energy in the 3×3 “patch” of towers surrounding and including the high energy tower to be above a second threshold. Although hardware thresholds varied over the course of the data taking, the analysis included an emulated trigger requirement, with thresholds of 4.3 and 6.2 GeV, respectively, for the high energy tower and the 3×3 tower patch. These emulated trigger thresholds were 10% above the maximum hardware triggers. π^0 candidates with p_T below the software energy threshold can arise from several sources, e.g., the spread and offset from the nominal longitudinal position of the collision vertex, off-line rejection from the π^0 candidate of hadronic energy deposits, and events with π^0 candidates not associated with the tower or tower clusters firing the trigger.

To understand the effects of backgrounds, efficiencies, and p_T resolution, data have been compared to a Monte Carlo simulation based on PYTHIA, as described previously, with GEANT 3.21 [41] to model detector response. An example of the data–Monte Carlo studies is shown in Fig. 2. In this example, distributions are compared between two-photon invariant mass and single-photon energy for two-photon events with a reconstructed transverse momentum range of $7 < p_T < 8$ GeV/c. In general, data and Monte Carlo distributions show reasonable agreement for $p_T > 6$ GeV/c. For $p_T < 6$ GeV/c, discrepancies between data and Monte Carlo lead to increased, but well-constrained systematic uncertainties in the estimation of signal fractions.

The signal fraction was determined by fitting a linear combination of template functions to the two-photon invariant mass distribution over the range $0 < M_{\gamma\gamma} < 0.3$ GeV/c²

for each p_T (or x_F) bin. Three template functions were determined by fitting the functions to Monte Carlo data to represent (a) the π^0 signal, (b) the conversion background where the two reconstructed “photons” that formed the π^0 candidate were actually the two leptons from a photon that converted in material upstream of the EEMC, and (c) all other backgrounds, including combinatoric backgrounds. Signal and conversion background events were determined by matching the momentum direction of reconstructed pairs to that of generated π^0 's and decay photons, respectively, in (η, φ) space. Nonmatched reconstructed pairs were considered “other” backgrounds. The shapes of the template functions were chosen to match the shapes of the various contributions from Monte Carlo. For the π^0 signal the sum of two skewed Gaussian distributions was chosen, while the two background contributions were each represented by single skewed Gaussian distributions. The parameter values were fixed by fitting the template functions to the contributions in Monte Carlo, and the relative weights of the templates were determined by fitting a linear combination of the template functions to the data. When fitting the weights of the three template functions an additional factor was also included to account for the energy scale difference between the data and the Monte Carlo. This energy scale difference was not simply related to the calibration but was also affected by assumptions about the sampling fraction used in the simulation. The energy scale difference extracted from the fits is approximately 3%.

The data and template functions for the $7 < p_T < 8$ GeV/c bin are shown in Fig. 3. While the fits to determine the signal fraction cover $0 < M_{\gamma\gamma} < 0.3$ GeV/c², only π^0 candidates with $M_{\gamma\gamma}$ in the range $0.1 < M_{\gamma\gamma} < 0.2$ GeV/c² (defined as the peak region) were used for the remainder of the analysis. The signal fraction in the peak region (Fig. 4) was computed from the weights, the data versus simulation energy scale factor, and integrals of the template functions. The product of the signal fraction

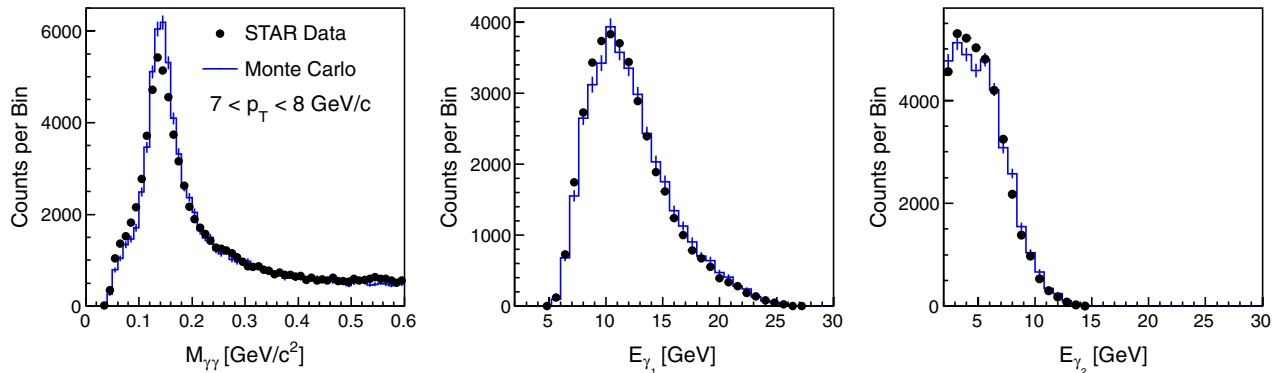


FIG. 2 (color online). Comparison of data to Monte Carlo for the distributions of two-photon invariant mass (left) and energy for the higher (center) and lower (right) energy photon. Distributions are shown with a reconstructed transverse momentum range of $7 < p_T < 8$ GeV/c. For the photon-energy distributions, a two-photon mass requirement of $0.1 < M_{\gamma\gamma} < 0.2$ GeV/c² is applied. The Monte Carlo distributions have been normalized to the number of counts in the data distributions.

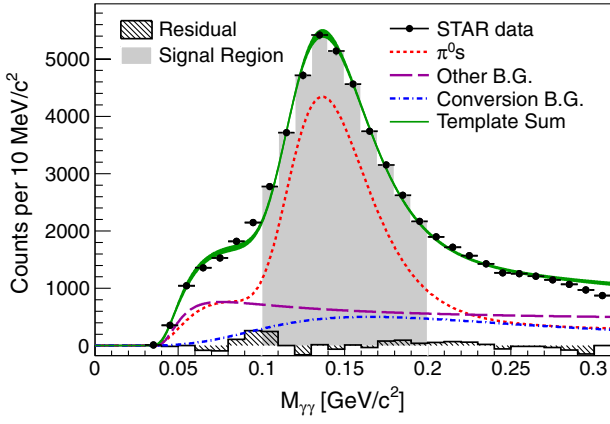


FIG. 3 (color online). Invariant mass distribution for the two-photon system with $7 < p_T < 8$ GeV/c. Also included on the plot are the template functions for the signal and two backgrounds (scaled and shifted according to the fit results), the residual between the data and the sum of the templates, and a gray-shaded area indicating the peak region.

in the peak region and the number of π^0 counts within this region then gives the number of background-subtracted π^0 's for the given bin.

To compute the cross section, the number of background-subtracted π^0 's was corrected for p_T bin smearing by applying the inverse of a smearing matrix, obtained from the same PYTHIA Monte Carlo data set as used above. The final cross section was then computed using

$$E \frac{d^3\sigma}{dp^3} = \frac{1}{\Delta\phi} \frac{1}{\Delta\eta} \frac{1}{\Delta p_T} \frac{1}{\langle p_T \rangle} \frac{1}{\text{BR}} \frac{1}{\epsilon} \frac{1}{\mathcal{L}}, \quad (2)$$

where N is the corrected number of π^0 's, \mathcal{L} is the sampled luminosity (including dead-time corrections), ϵ is the

product of reconstruction and trigger efficiencies, BR is the branching ratio $\pi^0 \rightarrow \gamma\gamma$ [42], $\langle p_T \rangle$ is the average p_T for the particular p_T bin, Δp_T is the width of the p_T bin, and $\Delta\phi$ (equal to 2π) and $\Delta\eta$ (equal to 1.2) are the ϕ and η phase space factors, respectively. The trigger efficiency is below 10% for π^0 's with $5 < p_T < 6$ GeV/c and plateaus above 40% at $p_T \approx 9$ GeV/c. The reconstruction efficiency is around 30% for $5 < p_T < 9$ GeV/c and decreases to around 20% for $12 < p_T < 16$ GeV/c.

The longitudinal spin asymmetries were computed by subtracting the luminosity asymmetry from the asymmetry in the number of π^0 candidates and dividing this difference by the luminosity-weighted polarization. Specifically, one can write

$$A_{LL} = \frac{1}{\langle P_B P_Y \rangle} \left(\frac{N^{++} - N^{+-} - N^{-+} + N^{--}}{N^{++} + N^{+-} + N^{-+} + N^{--}} - \frac{L^{++} - L^{+-} - L^{-+} + L^{--}}{L^{++} + L^{+-} + L^{-+} + L^{--}} \right), \quad (3)$$

$$A_{L,B} = \frac{1}{\langle P_B \rangle} \left(\frac{N^{++} + N^{+-} - N^{-+} - N^{--}}{N^{++} + N^{+-} + N^{-+} + N^{--}} - \frac{L^{++} + L^{+-} - L^{-+} - L^{--}}{L^{++} + L^{+-} + L^{-+} + L^{--}} \right), \quad (4)$$

$$A_{L,Y} = \frac{1}{\langle P_Y \rangle} \left(\frac{N^{++} - N^{+-} + N^{-+} - N^{--}}{N^{++} + N^{+-} + N^{-+} + N^{--}} - \frac{L^{++} - L^{+-} + L^{-+} - L^{--}}{L^{++} + L^{+-} + L^{-+} + L^{--}} \right). \quad (5)$$

Here, subscripts B and Y represent the blue (momentum from the interaction region towards the EEMC) and yellow

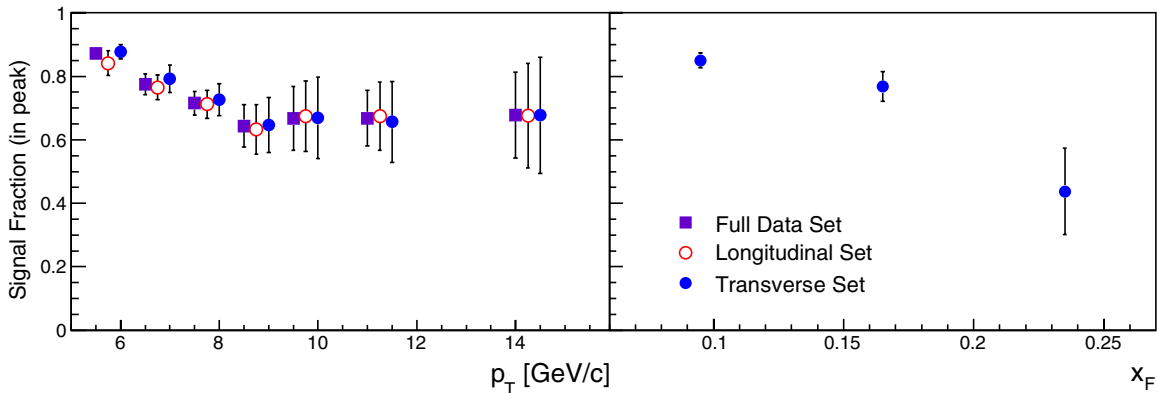


FIG. 4 (color online). Signal fractions calculated within the “peak region” of $0.1 < M_{\gamma\gamma} < 0.2$ GeV/c². Fractions for the full data set as well as the subsets of longitudinal and transverse polarizations are shown as a function of p_T (left), and the fractions for the transversely polarized data are shown as a function of x_F integrated over $5 < p_T < 12$ GeV/c (right). Uncertainties on the signal fractions arise from those of the template forms determined from Monte Carlo and from their application to the data. The size of the uncertainties is influenced by the number of events in the available data and Monte Carlo and the quality of fits to Monte Carlo and data. The same Monte Carlo sample is used to extract the signal fractions for the three data sets.

(momentum aimed away from the EEMC) beams, N denotes the number of counts in the signal region, and L indicates the luminosity. The superscripts $+$ and $-$ designate the longitudinal polarization directions of the blue beam and yellow beams, respectively. Equations (3)–(5) assume negligible contributions from terms of the form

$$A_{L,B} \times \frac{L^{++} - L^{--} - L^{+-} + L^{-+}}{L^{++} + L^{--} + L^{+-} + L^{-+}} \quad (6)$$

(similarly for $A_{L,Y}$) and also from terms coupling A_{LL} to the luminosity asymmetry. Luminosity asymmetries are kept quite small due to the ability of RHIC to alternate spin directions for successive bunch patterns using a complex eight-bunch polarization pattern. Since the parity-violating asymmetry A_L is expected to be quite small, these correction terms are considered negligible. The spin-dependent luminosities are calculated from the sum of BBC coincidences over a run, after sorting bunches for each spin combination. The luminosity-weighted average polarizations for the longitudinally polarized data have values $\langle P_B \rangle = 0.56$ and $\langle P_Y \rangle = 0.59$, and the luminosity-weighted average product of the polarizations has the value $\langle P_B P_Y \rangle = 0.33$. The relative polarization uncertainty of each beam is 4%, and the relative uncertainty for the product is 6%.

The signal fraction was determined using data summed over the spin states. The asymmetries were corrected for the background asymmetry using

$$A^{\text{sig}} = \frac{1}{s} (A^{\text{raw}} - (1-s)A^{\text{bkg}}), \quad (7)$$

where s is the signal fraction, A^{sig} is the asymmetry of the π^0 signal, A^{raw} is the asymmetry value before background subtraction [Eqs. (3)–(5)], and A^{bkg} is an estimate of the background asymmetry. The background asymmetries were estimated as the average of the p_T -integrated asymmetries in two sideband regions ($0 < M_{\gamma\gamma} < 0.1 \text{ GeV}/c^2$ and $0.2 < M_{\gamma\gamma} < 0.3 \text{ GeV}/c^2$) and were found to be less than 1σ from zero, with $\sigma \approx 0.01$.

The transverse spin asymmetry was computed by binning with respect to ϕ , the angle between the azimuthal angles of the π^0 and the spin polarization vector. The raw cross ratio $\mathcal{E}(\phi)$ was computed per ϕ bin:

$$\mathcal{E}(\phi) = \frac{\sqrt{N^\uparrow(\phi)N^\downarrow(\phi+\pi)} - \sqrt{N^\downarrow(\phi)N^\uparrow(\phi+\pi)}}{\sqrt{N^\uparrow(\phi)N^\downarrow(\phi+\pi)} + \sqrt{N^\downarrow(\phi)N^\uparrow(\phi+\pi)}}, \quad (8)$$

where N represents the number of counts, \uparrow denotes beam spin polarized vertically upward in the lab frame, and \downarrow denotes beam spin polarized vertically downward in the lab frame. The quantity $\mathcal{E}(\phi)$ was fit to the equation $C + \varepsilon \sin \phi$, the background was subtracted using Eq. (7) with $A^{\text{raw}} = \varepsilon$, and the final result for A_N was

obtained by dividing by the luminosity-weighted polarization. The luminosity-weighted average polarizations for the transversely polarized data have values $\langle P_B \rangle = 0.54$ and $\langle P_Y \rangle = 0.55$. The uncertainty due to propagation of the relative polarization uncertainty of each beam is 4% [43]. The background asymmetries were estimated as the average of the asymmetry in the two sideband regions and were found for both A_N and A_{LL} to be less than 1σ from zero, again with $\sigma \approx 0.01$.

III. RESULTS

A. Cross section

Figure 5 presents the measured cross section for neutral pions produced over the transverse momentum range $5 < p_T < 16 \text{ GeV}/c$. Contributions to the systematic uncertainties include those related to the uncertainty on the signal fraction, the smearing matrix, the effect of repeating the analysis with an additional $4 < p_T < 5 \text{ GeV}/c$ bin, the reconstruction and trigger efficiencies, the EEMC energy resolution, and the overall EEMC energy scale. The signal fraction uncertainty includes contributions from the uncertainties on the parameters in the template functions, the uncertainty on the weights of the templates, the uncertainty on the scale parameter and its effect on the integrals used to determine the signal fraction in the peak, and a contribution based on the integral of the residual in the signal region. Uncertainty on the luminosity results in a 7.7% vertical scale uncertainty. The dominant uncertainty

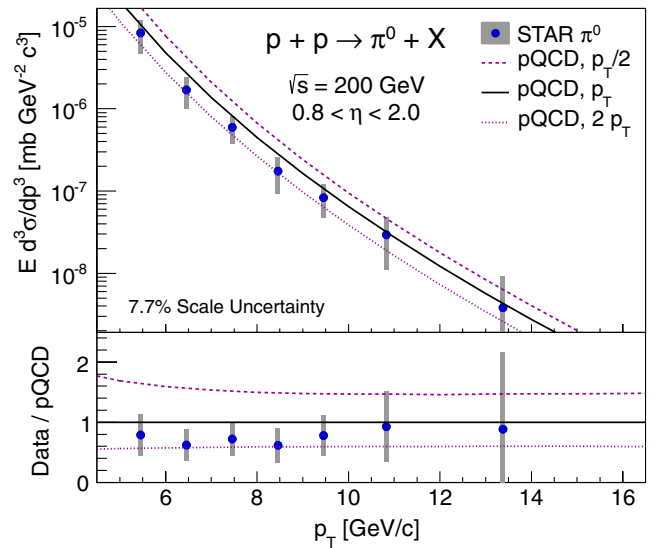


FIG. 5 (color online). Upper panel: The π^0 cross section (blue markers) is shown compared with an NLO pQCD calculation [1] with three options for the scale parameter. Statistical uncertainties are shown by the error bars which are indistinguishable from the markers in all bins. Systematic uncertainties are shown by the error boxes. The lower panel presents the ratio of the data to the p_T -scale theory curve, as well as the ratio of the $2p_T$ -scale and $p_T/2$ -scale theory curves to the p_T -scale curve.

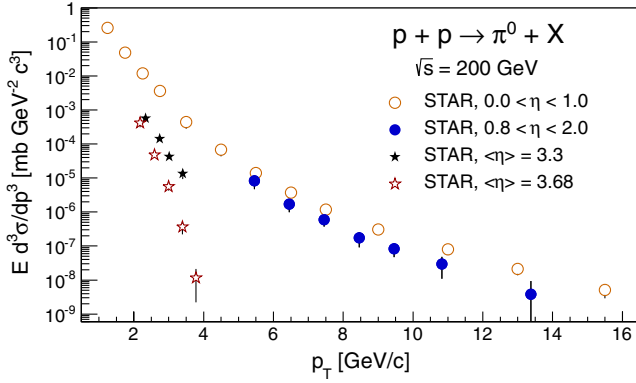


FIG. 6 (color online). The π^0 cross section at various ranges of pseudorapidity as measured by STAR. Error bars indicate the total uncertainty. The closed blue circles are the results of this analysis, while the other points are previously published results that use the STAR barrel electromagnetic calorimeter (open orange circles) [7] and the forward pion detectors (closed black stars and open red stars) [12,13].

on the cross section is the overall energy scale uncertainty, which is correlated over all bins.

The measured cross section results in Fig. 5 are compared to a theory prediction based on next-to-leading order (NLO) pQCD and global fits of distribution and fragmentation functions [1]. The CTEQ6.5 set of parton distribution functions [45] and de Florian-Sassot-Stratmann (DSS) fragmentation functions [14] are used. The EEMC π^0 cross section data points are observed to lie between the calculations that set the factorization, renormalization, and fragmentation scales to p_T and $2p_T$. This is qualitatively consistent with central pseudorapidity measurements from PHENIX, both in published results at $\sqrt{s} = 200$ GeV [4] and preliminary results at $\sqrt{s} = 500$ GeV [15]. In each of these measurements, the cross section is lower than the p_T -scale theory curve in the region of $5 < p_T < 16$ GeV/ c . Within uncertainties, previous STAR results at $\sqrt{s} = 200$ GeV are in good agreement with the p_T -scale theory predictions [7].

Figure 6 shows the cross section results of this analysis in comparison with previously published STAR results in other pseudorapidity and transverse-momentum regions. While the entire STAR detector has a broad range of coverage, the results presented here lie in a previously unmeasured region. The results indicate that the cross section changes slowly with respect to η at lower η and has significant η dependence at higher η , with the transition lying between $\eta = 2$ and $\eta = 3.3$.

B. Longitudinal asymmetries

The A_{LL} results for $5 < p_T < 12$ GeV/ c are shown in Fig. 7. Systematic uncertainties include those on the signal fraction and on the estimate of the background asymmetry. The relative luminosity uncertainty was found to be

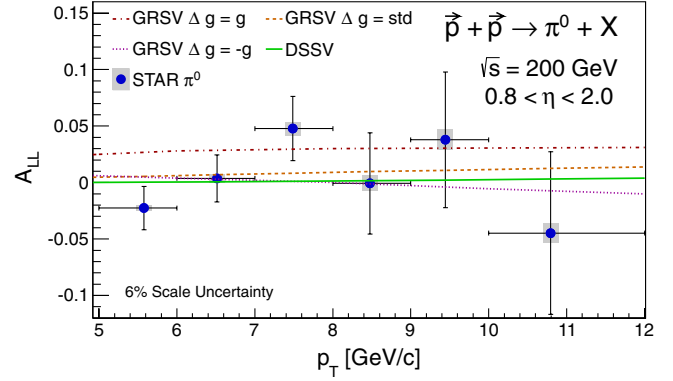


FIG. 7 (color online). The A_{LL} results (blue markers) are presented with the DSSV prediction [17] and the GRSV prediction [44] using the best fit to polarized DIS ($\Delta g = \text{std}$) and the maximum and minimum allowed values for gluon polarization. Statistical uncertainties are shown by the error bars, whereas systematic uncertainties are indicated by the error boxes. The 6% scale uncertainty is due to beam polarization uncertainty.

negligible compared to the systematic uncertainties from the signal fraction and the background asymmetry. Integrating over $5 < p_T < 12$ GeV/ c yields a value of $A_{LL} = 0.002 \pm 0.012$. Uncertainty in the product of beam polarizations results in a 6% vertical scale uncertainty as indicated in the figure. This systematic uncertainty is correlated across all bins and vanishes as the measured asymmetries go to zero.

Model predictions, based on global fits by the Glück-Reya-Stratmann-Vogelsang (GRSV) group to polarized deep inelastic scattering (DIS) data [44] and global fits by the de Florian-Sassot-Stratman-Vogelsang (DSSV) group to polarized DIS, semi-inclusive DIS, and proton-proton collisions [17], are shown along with the measured A_{LL} results in Fig. 7. For the GRSV prediction, calculations are shown for the best fit to polarized DIS ($\Delta g = \text{std}$) as well as those for the maximum ($\Delta g = g$) and minimum ($\Delta g = -g$) allowed gluon polarization. Both GRSV and DSSV are calculated at NLO. DSS fragmentation functions [14] are utilized, as well as the CTEQ6.5 set of parton distribution functions [45] with the unpolarized NLO calculation [1]. The A_{LL} results lack the precision to distinguish between the present various parameterizations of gluon polarization yet may still impact global extractions of $\Delta g(x)$ which reach to less-constrained values of low Bjorken- x or those not presently including RHIC data (e.g., Ref. [46]).

The parity-violating single-spin asymmetry A_L was also measured for each of the colliding beams and is consistent with zero. Integrating over p_T from $5 < p_T < 12$ GeV/ c yields $A_L = -0.003 \pm 0.007$ (blue beam) and $A_L = -0.001 \pm 0.007$ (yellow beam).

C. Transverse spin asymmetries

The results for A_N versus x_F , integrated over $5 < p_T < 12$ GeV/ c , as well as A_N versus p_T , integrated

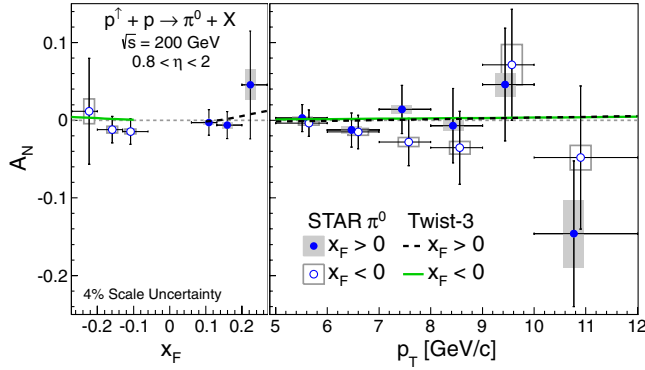


FIG. 8 (color online). The A_N results are plotted versus x_F integrated over $5 < p_T < 12$ GeV/c (left panel) and versus p_T integrated over $0.06 < |x_F| < 0.27$ (right panel). Statistical uncertainties are shown by error bars, whereas systematic uncertainties are indicated by error boxes. Negative x_F results are depicted with open circles and open error boxes, while positive x_F results are exhibited with closed circles and closed systematic error boxes. The A_N results are presented with model predictions based on the twist-3 mechanism in the collinear factorization framework [34]. The 4% scale uncertainty is due to beam polarization uncertainty.

over $0.06 < |x_F| < 0.27$, are shown in Fig. 8. Asymmetries for $x_F > 0$ are measured accounting for the polarization direction of the blue beam, while those for $x_F < 0$ are measured accounting for that of the yellow beam. Systematic uncertainties include those on the signal fraction, on the estimate of the background asymmetry, and on single-beam backgrounds. Uncertainty in the beam polarizations results in a 4% vertical scale uncertainty as

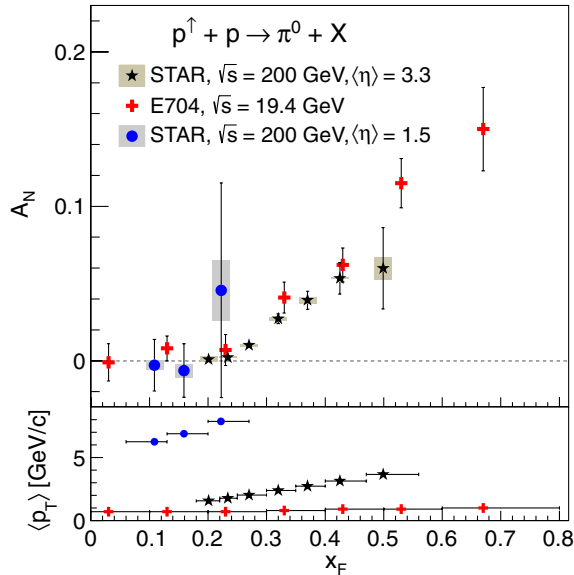


FIG. 9 (color online). The present A_N results (blue circles) are compared with previously published values of A_N [9,23] as a function of x_F (top panel). The average p_T values within each x_F bin are compared for the various measurements (bottom panel).

indicated in the figure. Over the x_F region of this measurement, A_N is statistically consistent with zero and no strong conclusions about the p_T dependence can be made. The measured asymmetries are presented with model predictions based on the twist-3 mechanism in the collinear factorization scheme [34]. The measured asymmetries are consistent with the model predictions which expect small effects for both $x_F > 0$ and $x_F < 0$.

The present A_N results are compared with previously published results in Fig. 9. The lower panel of Fig. 9 shows the average p_T for each bin of x_F . As anticipated from the previous results at lower p_T and similar x_F [9,11,23–25], A_N is statistically consistent with zero. Integrating over $0.06 < |x_F| < 0.27$ over the aforementioned range of p_T yields $A_N = 0.000 \pm 0.009$ for $x_F > 0$ and $A_N = 0.009 \pm 0.009$ for $x_F < 0$, with $\langle |x_F| \rangle = 0.14$.

IV. CONCLUSIONS

Neutral pions produced from polarized proton-proton collisions with $\sqrt{s} = 200$ GeV at RHIC have been detected using the STAR end cap electromagnetic calorimeter. The production cross section, the longitudinal double- and single-spin asymmetries, and the transverse single-spin asymmetry have been measured for π^0 's with $0.8 < \eta < 2.0$. The spin asymmetries were extracted for π^0 's over the range $5 < p_T < 12$ GeV/c, while the cross section was measured for those over the range $5 < p_T < 16$ GeV/c. These results probe a region of phase space not previously studied at RHIC energies, complementing measurements in neighboring regions. The cross section is slightly lower than previously published measurements at more central ranges of pseudorapidity and within the scale uncertainty of a pQCD-calculated prediction. The A_{LL} measurement is compared with a model prediction and includes data with Bjorken- x_2 reaching below 0.01 based on calculations utilizing unpolarized parton distribution functions. The measured values of the parity-violating spin asymmetry A_L are consistent with zero. The measured values of A_N are compared with a twist-3 model prediction and found to be consistent. The present results are also compared with previously published measurements which also suggest small asymmetries for similar x_F and lower values of p_T .

ACKNOWLEDGMENTS

The authors thank M. Stratmann, W. Vogelsang, and K. Kanazawa for providing calculations and discussion. We thank the RHIC Operations Group and RCF at BNL, the NERSC Center at LBNL, the KISTI Center in Korea and the Open Science Grid consortium for providing resources and support. This work was supported in part by the Offices of NP and HEP within the U.S. DOE Office of Science, the U.S. NSF, CNRS/IN2P3, FAPESP CNPq of Brazil, Ministry of Education and Science of the Russian Federation, NNSFC, CAS, MoST and MoE of

China, the Korean Research Foundation, GA and MSMT of the Czech Republic, FIAS of Germany, DAE, DST, and CSIR of India, National Science Centre of Poland, National Research Foundation (NRF-2012004024), Ministry of

Science, Education and Sports of the Republic of Croatia, and RosAtom of Russia. Finally, we gratefully acknowledge a sponsored research grant for the 2006 run period from Renaissance Technologies Corporation.

-
- [1] B. Jäger, A. Schäfer, M. Stratmann, and W. Vogelsang, *Phys. Rev. D* **67**, 054005 (2003).
- [2] B. Jäger, M. Stratmann, and W. Vogelsang, *Phys. Rev. D* **70**, 034010 (2004).
- [3] S. Kretzer, *Acta Phys. Pol. B* **36**, 179 (2005); C. Aidala *et al.*, Research Plan for Spin Physics at RHIC (2005), <http://spin.riken.bnl.gov/rsc/report/masterspin.pdf>.
- [4] S. S. Adler *et al.* (PHENIX Collaboration), *Phys. Rev. Lett.* **91**, 241803 (2003); (PHENIX Collaboration), *Phys. Rev. Lett.* **98**, 172302 (2007); A. Adare *et al.* (PHENIX Collaboration), *Phys. Rev. D* **76**, 051106(R) (2007).
- [5] S. S. Adler *et al.* (PHENIX Collaboration), *Phys. Rev. Lett.* **93**, 202002 (2004); (PHENIX Collaboration), *Phys. Rev. D* **73**, 091102(R) (2006); A. Adare *et al.* (PHENIX Collaboration), *Phys. Rev. Lett.* **103**, 012003 (2009).
- [6] S. Adler *et al.* (PHENIX Collaboration), *Phys. Rev. Lett.* **95**, 202001 (2005).
- [7] B. I. Abelev *et al.* (STAR Collaboration), *Phys. Rev. D* **80**, 111108(R) (2009).
- [8] B. I. Abelev *et al.* (STAR Collaboration), *Phys. Rev. C* **81**, 064904 (2010).
- [9] B. E. Bonner *et al.* (FNAL-E704 Collaboration), *Phys. Rev. Lett.* **61**, 1918 (1988); D. L. Adams *et al.* (FNAL-E581/E704 Collaboration), *Phys. Lett. B* **261**, 197 (1991).
- [10] D. L. Adams *et al.* (FNAL-E581/E704 Collaboration), *Phys. Lett. B* **261**, 201 (1991).
- [11] J. Adams *et al.* (STAR Collaboration), *Phys. Rev. Lett.* **92**, 171801 (2004).
- [12] J. Adams *et al.* (STAR Collaboration), *Phys. Rev. Lett.* **97**, 152302 (2006).
- [13] L. Adamczyk *et al.* (STAR Collaboration), *Phys. Rev. D* **86**, 051101(R) (2012).
- [14] D. de Florian, R. Sassot, and M. Stratmann, *Phys. Rev. D* **75**, 114010 (2007).
- [15] A. Bazilevsky (PHENIX Collaboration), in \sqrt{s} dependence of π^0 production in pp collisions at midrapidity from PHENIX (2010), presented at the American Physical Society, Spring Meeting, <http://www.phenix.bnl.gov/phenix/WWW/talk/archive/2010/APS10/t1634.ppt>.
- [16] J. Babcock, E. Monsay, and D. Sivers, *Phys. Rev. Lett.* **40**, 1161 (1978); *Phys. Rev. D* **19**, 1483 (1979); G. Bunce, N. Saito, J. Soffer, and W. Vogelsang, *Annu. Rev. Nucl. Part. Sci.* **50**, 525 (2000).
- [17] D. de Florian, R. Sassot, M. Stratmann, and W. Vogelsang, *Phys. Rev. Lett.* **101**, 072001 (2008).
- [18] E. Aschenauer *et al.* (RHIC Spin Collaboration), arXiv:1304.0079.
- [19] T. Sjöstrand, S. Mrenna, and P. Skands, *J. High Energy Phys.* **05** (2006) 026.
- [20] P. Z. Skands, *Phys. Rev. D* **82**, 074018 (2010).
- [21] H. L. Lai, J. Huston, S. Kuhlmann, J. Morfin, F. Olness, J. F. Owens, J. Pumplin, and W. K. Tung, *Eur. Phys. J. C* **12**, 375 (2000).
- [22] L. Adamczyk *et al.* (STAR Collaboration), *Phys. Rev. D* **86**, 032006 (2012).
- [23] B. I. Abelev *et al.* (STAR Collaboration), *Phys. Rev. Lett.* **101**, 222001 (2008).
- [24] J. L. Drachenberg (STAR Collaboration), *AIP Conf. Proc.* **1149**, 517 (2009); N. Poljak (STAR Collaboration), *ibid.* **1149**, 521 (2009); A. Ogawa (STAR Collaboration), *ibid.* **1182**, 561 (2009); G. Igo (STAR Collaboration), *ibid.* **1523**, 188 (2013); S. Heppelmann (STAR Collaboration), *Proc. Sci.*, DIS2013 (2013) 240.
- [25] A. Adare *et al.* (PHENIX Collaboration), arXiv:1312.1995.
- [26] D. Sivers, *Phys. Rev. D* **41**, 83 (1990); *Phys. Rev. D* **43**, 261 (1991).
- [27] J. Collins, *Nucl. Phys.* **B396**, 161 (1993).
- [28] U. D'Alesio, F. Murgia, and C. Pisano, *Phys. Rev. D* **83**, 034021 (2011).
- [29] M. Anselmino, M. Boglione, U. D'Alesio, S. Melis, F. Murgia, and A. Prokudin, *Phys. Rev. D* **88**, 054023 (2013).
- [30] Z.-B. Kang and F. Yuan, *Phys. Rev. D* **84**, 034019 (2011).
- [31] A. Efremov and O. Teryaev, *Yad. Fiz.* **36**, 242 (1982) [*Sov. J. Nucl. Phys.* **36**, 140 (1982)]; *Phys. Lett.* **150B**, 383 (1985); *Phys. Lett. B* **348**, 577 (1995).
- [32] J. Qiu and G. Sterman, *Phys. Rev. D* **59**, 014004 (1998).
- [33] K. Kanazawa and Y. Koike, *Phys. Rev. D* **82**, 034009 (2010).
- [34] K. Kanazawa and Y. Koike, *Phys. Rev. D* **83**, 114024 (2011).
- [35] G. L. Kane, J. Pumplin, and W. Repko, *Phys. Rev. Lett.* **41**, 1689 (1978).
- [36] C. Kouvaris, J.-W. Qiu, W. Vogelsang, and F. Yuan, *Phys. Rev. D* **74**, 114013 (2006).
- [37] K. Ackermann *et al.* (STAR Collaboration), *Nucl. Instrum. Methods Phys. Res., Sect. A* **499**, 624 (2003).
- [38] M. Anderson *et al.*, *Nucl. Instrum. Methods Phys. Res., Sect. A* **499**, 659 (2003).
- [39] J. Kiryluk (STAR Collaboration), *AIP Conf. Proc.* **675**, 424 (2003); J. Adams *et al.* (STAR Collaboration), *Phys. Rev. Lett.* **91**, 172302 (2003).
- [40] C. Allgower *et al.*, *Nucl. Instrum. Methods Phys. Res., Sect. A* **499**, 740 (2003).
- [41] R. Brun *et al.*, GEANT3, Report No. CERN-DD-EE-84-1, 1987; R. Brun, F. Carminati, and S. Giani, GEANT Detector

- Description and Simulation Tool, Reports No. CERN-W5013 and No. CERN-W-5013, 1994.
- [42] J. Beringer *et al.* (Particle Data Group), *Phys. Rev. D* **86**, 010001 (2012).
- [43] A. Bazilevsky, (RHIC CNI Group) Run6 CNI Analysis: Concluding Remarks and Summary of Systematic Uncertainties, http://www4.rcf.bnl.gov/~cnipol/pubdocs/Run06Offline/RSC_30nov2007_sasha.ppt; RHIC CNI Group, 2006 Polarizations for RHIC, http://www4.rcf.bnl.gov/~cnipol/pubdocs/Run06Offline/NOTE_2006_Polarizations_RHIC.txt.
- [44] M. Glück, E. Reya, M. Stratmann, and W. Vogelsang, *Phys. Rev. D* **63**, 094005 (2001).
- [45] W. K. Tung, H. L. Lai, A. Belyaev, J. Pumplin, D. Stump, and C.-P. Yuan, *J. High Energy Phys.* **02** (2007) 053.
- [46] R. D. Ball, S. Forte, A. Guffanti, E. R. Nocera, G. Ridolfi, J. Rojo (NNPDF Collaboration), *Nucl. Phys.* **B874**, 36 (2013).